Gold Nanoparticle Superlattices: Conditions for Long-Range Order, Moiré Patterns, and Binary Phase from a Single Population

Chiara Moretti, Claire Goldmann, Marianne Imperor-Clerc, Benjamin Abécassis

Gold nanoparticle superlattices: conditions for long range order, Moiré patterns and binary phase from a single population

Chiara Moretti[1], Claire Goldman[2], Marianne Imperor-Clerc[2], and Benjamin Abécassis[1,✉]

[1]ENSL, CNRS, Laboratoire de Chimie UMR 5182, 46 allée d'Italie, 69364 Lyon France
[2]Laboratoire de Physique des Solides, Université Paris-Saclay, CNRS, 91405 Orsay

We report the two-dimensional self-assembly at the liquid-air interface of spherical gold nanoparticles (NPs) with diameters between 2 and 14 nm. By exploring the self-assembly conditions, such as the dispersing solvent and the coating ligand (thiols with different lengths, oleylamine, polystyrene), we identify suitable conditions for long range close-packed monolayers obtention. We show that though NPs with diameters below 3 nm yield glassy films or fuse during self-assembly depending on the ligand length, NPs with larger sizes dispersed in toluene yield well-ordered monolayers over distances that can span tens of micrometers. Adding free ligand in solution before the self-assembly triggers long range ordering into close-packed structures of otherwise amorphous films. The equilibrium distance between the NPs within the monolayers are compared to predictions by the OPM and OCM geometrical models. We also observed a $CaCu_5$ phase in few-layers assemblies which results from the size segregation of a single monodisperse population of NPs into two populations of different mean sizes occupying the two different sites of this complex lattice. In some instances, Moiré patterns consisting of two close-packed hexagonal monolayers superimposed with a twist angle are evidenced. By comparing the experimental structures with numerically simulated patterns, we show that a twist angle of 30° yields a quasicrystalline order with a 12-fold rotational symmetry. Our work provides insights into fundamental processes behind the self-assembly of colloidal nanocrystals into ordered mono- and few-layers as well as more complex assemblies such as quasicrystalline or Frank-Kasper phases. These structures are of great significance for bottom-up fabrication of functional devices that advantage of (collective) plasmonics properties or surface enhanced raman scattering.

gold nanoparticle| self-assembly | superlattices | liquid-liquid interface | Frank Kasper Phases | Quasi-crystals

Correspondence: *benjamin.abecassis@ens-lyon.fr*

Introduction

NP self-assembly is a very versatile mean to create new materials with unique and tunable properties by exploiting a wide variety of combinations of particle size, shape and composition (1, 2). NPs can self-assemble into long-range ordered structures, such as 2D- and 3D-superlattices with very different crystal structures from which new collective properties can emerge. (3). A broad range of superlattices have been discovered from the self-assembly of metal (4), metal oxide (5), chalcogenide (6), core-shell (7), semiconductor NPs (8) and binary systems (9–11). Among these different materials, gold NPs can serve as a model system since they have original plasmonic properties that depend on their organization (12). Furthermore, there is now an excellent control over their mean size, size distribution, shape and surface modification. Monodisperse spherical gold NPs can self-assemble in cubic or hexagonal close-packed symmetries (13). The first large (> 20 μm) hexagonal close-packed film composed of 7 nm thiolated-gold NPs was reported by Eah *et al.* (14). Gold NPs with diameters over 12 nm, stabilized by polystyrene-based ligands, form very large well-ordered monolayers (4). Small 2 nm gold NPs can also assemble in 3D into more complex structure such as Frank-Kasper phases (15). Thin films of self-assembled gold nanoparticles can be exploited in several applications, such as electronics (16), data storage (17) and plasmonics (18). For example, doping a film composed of semi-conducting nanoparticles with gold NPs was shown to impact strongly their transport properties (19). Strong light matter coupling has been observed in self-assembled films of gold nanoparticles (12). Nevertheless, for these purposes, long-range ordered areas of gold NPs are needed and are still challenging to obtain.

Among the different self-assembly methods, the evaporation of colloidal dispersions on a liquid substrate has recently emerged as an efficient way to produce monolayers in which the NPs organize into 2D superlattices (11). In this method, a colloidal dispersion of nanocrystals in a volatile solvent is deposited on a non volatile liquid such a di-ethylene glycol and allowed to evaporate. The density of the thin film increases and the NPs assemble at the triple line (liquid/liquid/air). During this process, both thermodynamic and kinetic factors have to be taken into account. The inter-particle interaction potential plays a key role in the final structure of the film but the speed at which the evaporation occurs is also important. For the maximum density and order to be achieved the NPs need to have time to re-arrange and to reach their ground state configuration which minimizes their interaction free energy.

The structural diversity in superlattices is due to the interplay of several inter-particle forces such as van der Waals, electrostatic, dipolar, depletion or steric hindrance (20). For pure monodisperse hard sphere systems, it has been known for more than 60 years that increasing the concentration of a dispersion results in a fluid-to-crystal transition. However, experimental conditions are often far from this ideal case. For example, any synthetic particles exhibit polydispersity

which has a strong tendency to suppress crystallization. The polydispersity threshold above which crystallization is canceled has been found theoretically to vary from 7% to 20% depending on the simulation technique (21–23). However, subpopulations of a polydisperse dispersion can segregate and crystallize under different phases (24). The interaction potential between the NPs is also more complex than pure hard sphere with softer components of various origins which favor less close packed structures. In the case of NPs, it is important to notice that the DLVO framework developed for micron sized colloids is only partially relevant at the nanoscale (25). Colloidal nanocrystals are coated with a monolayer of organic surfactants which play an important role in their their self-assembly behavior (26). Molecular dynamics simulations and experiments have shown that the ligand-ligand van der Waals (vdW) interactions dominate the interaction in solution for small particles with diameters below around 8 nm while for larger particles, the vdW interactions between two NPs prevail (27–29). This transition between ligand and core dominated regimes can be explained by the tendency of the ligands to bundle at the surface of the NP for small sizes. The anisotropic adsorption of the ligands at the NP surface favors the interlocking of the bundles. As NP size increases, this bundling is less favored by a lower curvature of the surface and interlocking decreases which results in a larger interparticle distance. In contrast, in the core dominated regime, interdigitation between ligands results in a larger compression of the shell which is not advantaged energetically and hence the interparticle distance decreases with increasing NP size. Several models have been designed to rationalize the packing of ligand coated NPs. In the Optimal Packing Model (OPM) (30–33), the ligand chain occupies a volume close to the one of fully extended chains. In the Overlap Cone Model (OCM), the ligands of neighboring NPs can overlap which allows to take into account many-body effects and thus better predict 2D self-assembly. (33).

Despite a large amount of work devoted to this field, the understanding of the conditions for assembly still needs satisfactory rationalization. More specifically, our understanding of the effect of self-assembly conditions in terms of NP shape, size, solvent, ligand coating which impact both the interaction between NPs and the self-assembly kinetics on the final self-assembled structures remains an unresolved question which begs further investigation. We investigated the 2D self-assembly of spherical gold NPs with well controlled sizes and polydispersity at the liquid/air interface to identify the main factors involved in this complex process. Our goal was to link the physico-chemical conditions to the structure of the assembly to identify the relevant parameters which tune the final organization of the NPs. We varied in a systematic fashion the size of the particles, the solvent and the length of the thiol ligand. We show that toluene is an adequate solvent for the formation of long ranged ordered films. Small NPs below 3 nm in diameter form films when coated with long ligands but did not display long range ordering. We identify conditions in which larger gold NPs form hexagonal films for all the other sizes and show that a small amount of free thiols in solution can induce ordering. The edge-to-edge distance shows that the ligands are highly interpenetrated within the monolayers. This observable also depends on the solvent, the size of the NPs and on the amount of added ligand prior to self-assembly. We also identified a binary $CaCu_5$ phase for 11 nm NPs coated with a polystyrene ligand in which size segregation occurs at different lattice sites. Several Moiré patterns resulting from the superposition of two twisted hexagonal close-packed layers are observed. We discuss our results in light of available models and show that further investigation in this area is needed. In this respect, our well calibrated experiments provide a foundation for future theories to predict the self-assembly of colloidal nanocrystals.

Results and discussion

To elucidate the 2D self-assembly of NPs at the liquid/air interface, we synthesized spherical gold NPs of varying sizes and surface functions by following different synthesis methods (see experimental methods for details). Our goal was to get a library of gold NPs with well-staggered sizes, different surface ligands and dispersible in hydrophobic volatile organic solvents. Table 1 reports the studied samples used for superlattice preparation with their mean diameters, relative standard deviation (RSD), both determined by TEM and SAXS (Fig. 1a and b), the capping ligands, the average edge-to-edge distance (d_e) between two NPs in a close-packed monolayer, and the solvent used for the self-assembly. In the following, we designate the NPs by their mean diameter as determined by TEM.

NPs with diameters between 3 and 5 nm were synthesized following a recently developed seeding growth synthesis (34), using small seeds of 2 nm obtained following the Brust method (35), which were regrown in a reaction medium containing a gold salt and an amine-borane complex as the reducing agent. Larger NPs with a mean diameter of around 6 nm were obtained by a one-phase method using an amine-borane complex as reducing agent (36). All these NPs, with a diameter ranging from 3 to 6.4 nm, were coated by 1-hexanedecanethiol and have a polydispersity smaller than 10%. The 2 nm NPs correspond to the seeds used in the seeded-growth synthesis and were coated either by 1-hexanethiol or 1-hexanedecanethiol. They have a slightly higher polydispersity with relative standard deviations of 13 and 15% (see Table 1). Another batch of NPs with 4.9 nm mean diameter was synthesized through a burst nucleation method upon injection of the reducing agent *tert*-butylamine-borane complex into a solution of gold salt, tetralin and oleylamine (OLA) (19), and the NPs were then coated by 1-dodecanethiol. By following the protocol described in Peng *et al.* (37), we synthesized 5.9 nm NPs coated with oleylamine. NPs with mean diameters larger than 8 nm were synthesized in aqueous medium and then transferred to organic solvents by a direct ligand exchange. For example, 9.4

d_T (nm)	RSD_T (%)	d_S (nm)	RSD_S (%)	d_e (nm)	Ligand	Solvent
/	/	2.0	15	/	C6-thiol	hexane, toluene
/	/	2.0	13	/	C16-thiol	hexane, toluene
3.0	5	3.0	9	1.2	C16-thiol	cyclohexane, toluene
4.0	5	4.0	9	1.3	C16-thiol	cyclohexane, toluene
5.0	5	5.1	7	1.6	C16-thiol	cyclohexane, toluene
6.0	6	6.2	9	/	C16-thiol	cyclohexane, toluene
6.4	4	6.6	10	1.7	C16-thiol	cyclohexane, toluene
4.9	5	5.4	8	1.9	C12-thiol	hexane
5.9	7	/	/	1.3	OLA	cyclohexane, hexane
9.4	6	9.1	4	2.5	PSSH	toluene
11.3	7	11.6	12	3.8	PSSH	toluene
14.0	5	13.0	14	1.4	OLA	toluene

Table 1. Au NP samples used for the 2D self-assembly experiments, reporting for each one the average core diameter and their RSD from TEM (d_T, RSD_T) and SAXS (d_S, RSD_S) analysis, the average edge-to-edge distance (d_e) between the NPs in the hexagonal packing, the capping ligand, and the solvent in which they were dispersed. The RSD is defined as the ratio of the standard deviation over the diameter.

nm NPs were synthesized from the growth of cetyltrimethylammonium bromide (CTAB)-capped Au cluster in an aqueous solution of cetyltrimethylammonium chloride (CTAC) and ascorbic acid by adding different volumes of $HAuCl_4$ solution (38). These NPs, initially coated by CTAC, were then functionalized with a thiol-terminated polystyrene ligand with a molecular weight of 2 kDa (PSSH) (39). Finally, NPs with diameters of 11.3 and 14 nm were synthesized by following a Turkevich protocol using a citrate buffer and a gold salt, as reported in (40). These NPs coated by citrate were then transferred in organic phase by a direct ligand exchange in toluene with OLA or PSSH (4).

All these NPs, were then dispersed in volatile organic solvents, such as hexane, cyclohexane and toluene for subsequent self-assembly. We employed a drying-mediated method to self-assemble the NPs at the liquid-air interface at room temperature (11), using a Teflon well as support and a non-volatile liquid sub-phase, diethylene glycol (DEG), as sketched in Fig. 1c. The gold NP concentration in the volatile solvent was adapted depending on the NP and the ligands so that, after evaporation, the area covered corresponds to a monolayer with an hexagonal dense packing (see the methods section for further details). In the following, we present the results of the self-assembly for NPs with increasing sizes. For each size, we changed the self-assembly conditions and discuss their effect on the self-assembled 2D film.

We first investigated the self-assembly of 2 nm NPs. We found that when coated with hexanethiol, the NPs aggregate and fuse due to their large surface area. We did not observe compact monolayers with either toluene or hexane (Fig. S1) but several types of assemblies such as large, thick and non-homogeneous aggregates of fused NPs (Fig. S1a,c). In other parts of the TEM grid, smaller spherical or ellipsoidal droplets with mean dimensions of about 30 nm are observed (Fig. S1b) while discrete NPs are seen in some instances (Fig. S1d).

Coating the same NPs with a longer ligand (1-hexadecanethiol) yields very extended thin films (Fig. S2a), with several cracks, which cover more than 4×10^3 μm^2. The film is composed of a monolayer or multilayers of NPs without any two-dimensional hexagonal packing (see Fig. S2b). This lack of symmetry may be due to their relatively high polydispersity (RSD of 15%) which might be too high to obtain self-assembled hexagonal superlattices. In contrast with hexanethiol coated NPs, they do not merge due to the longer carbon chain of the ligand which stabilizes them better and prevents their aggregation during self-assembly.

For larger NPs with diameters between 3 and 6.4 nm coated by 1-hexanedecanethiol, the structure of the film depends on the solvent. For toluene, evaporation of colloidal solutions yield extended and homogeneous films spanning tens of micrometers (Fig. S3-S7) which display long-ranged ordered monolayers with hexagonal close-packed symmetry, as confirmed by the Fourier transform (FT) of the TEM images. The structure of these films is detailed later in the paper. In contrast, when using cyclohexane instead of toluene for the same nanoparticles we observed less compact films displaying only small domains with hexagonal arrangement and short ranged order as monolayers or multi-layers depending on the region of the TEM grid (Fig. S8). This effect might be due to the slower evaporation rate of toluene which promotes a better organization during self-assembly. For the batch of NPs with the smallest polydispersity (RSD of 7% with mean diameter of 5 nm) we observed well organized films with a hexagonal symmetry using both solvents, pointing out the critical role of polydispersity in the self-assembly (Fig. S9).

For oleylamine coated NPs, the choice of the solvent affected the self-assembly in an even more critical fashion. Using hexane, oleylamine coated 5.9 nm NPs form extended films with different types of layers (Fig. S10). We found hexagonal multilayers and monolayers with defects, in which the NPs are organized in close-packed hexagonal lattices in small areas of around 6×10^3 nm^2. On the other hand, using cyclohexane, very extended films were also obtained, but without any long-range periodic organization. Additionally, some NPs have merged into irregular shapes ((Fig. S10b). This can be explained by the lower stability of oleylamine-coated Au

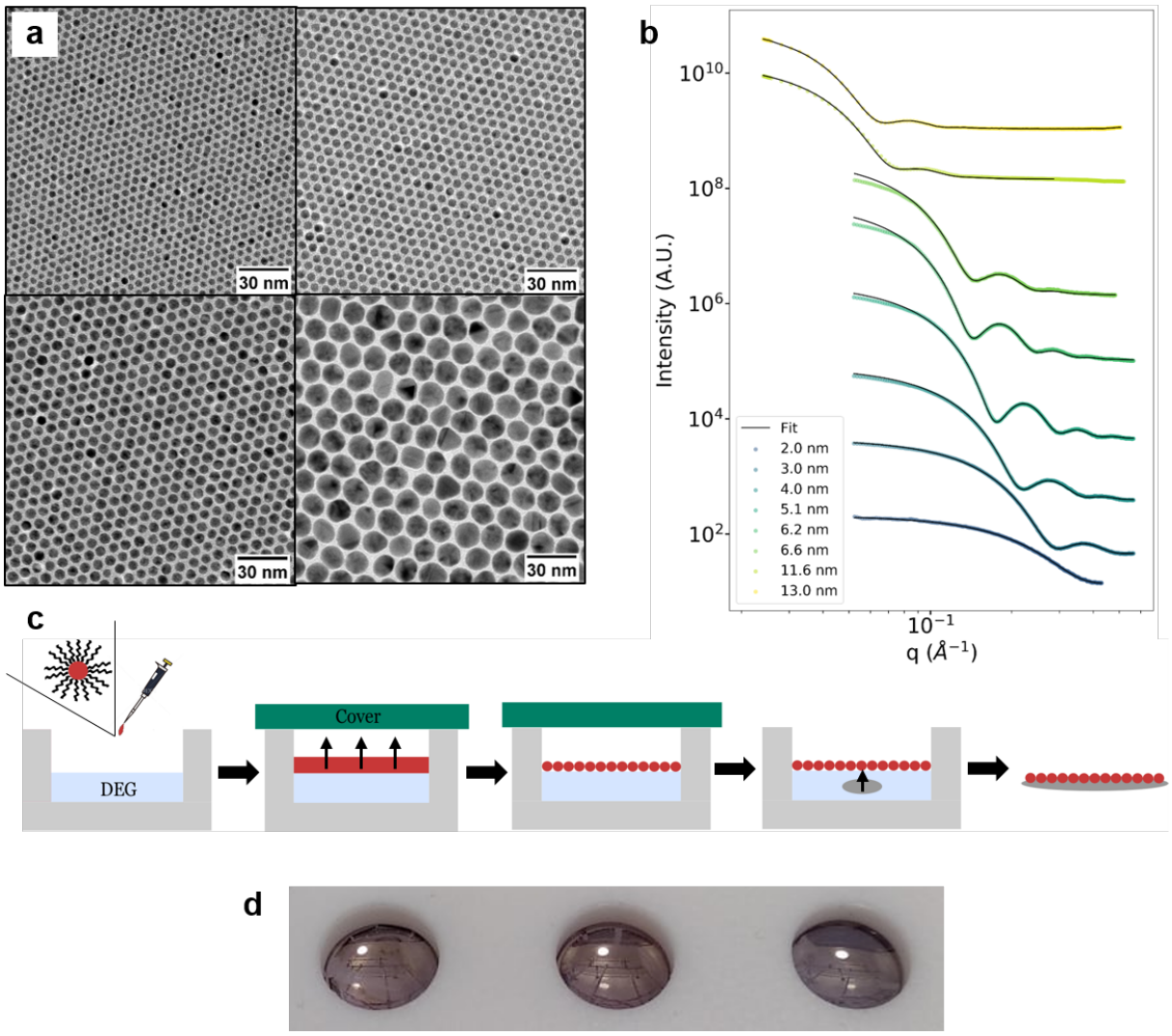

Fig. 1. a) TEM images of 4, 5, 6 and 14 nm Au NPs and (b) their SAXS diagrams fitted with a model of polydisperse spheres (solide black lines). c) Schematic of the 2D self-assembly at the liquid/air interface of NPs into superlattices using a Teflon well. d) NP thin films with mirror effect on DEG in the Teflon well after solvent evaporation.

NPs in cyclic solvent. Since the amine-gold bond is more labile than the thiol-gold bond (41), oleylamine forms a less rigid coating on the NP surface which can be more easily destabilized by the solvent and ultimately lead to their fusion (Fig. S11).

Once we had identified toluene as the best solvent to obtain well-ordered superlattices, we have performed the same self-assembly experiments using spherical gold NPs of different sizes from 3 to 6.4 nm.

They all form very extended films that span over several micrometers (Fig. 2) yielding high quality monolayers with less than 1% lacunae (see Methods for the measurement of lacunae percentage) and cracks, that are probably due to the film recovering method on the TEM grids by using tweezers. We observed qualitatively that as size increases the homogeneity of the film improves with less cracks or voids.

For 3 nm Au NPs we identify small areas in which the NPs don't form a monolayer but ramifications of different widths (from 10 to 200 nm) and small circular clusters of overlapped NPs (Fig. S4). In a few small areas of the TEM grid, the NPs merge and connect into small semi-continuous networks (composed of around 2-6 NPs) preserving the hexagonal symmetry. Monolayers of 4 nm NP also display small spherical clusters of overlapped NPs, with a diameter ranging from 30 to 150 nm, isolated or inside the monolayers (Fig. S5). Only a few NPs (around 1%) have merged. As size increases, the quality of the films gets better with 5.1 nm NPs forming extended hexagonal monolayers with only around 1% of lacunar defects (Fig. 2f and S6). In some part of the grid there are small areas in which the NPs are overlapped without any long-range organization.

6.4 nm Au NPs yield the most extended monolayers of the series (Fig. 2a-c): the well-ordered thin films cover thousands of square micrometers with around 1% of lacunar defects and display hexagonal close-packed structure. Overall, as the NP size increases between 3 and 6.4 nm, the range of the hexagonal order increases as proven by the higher and higher number of orders in the FT of the images (Fig. 2).

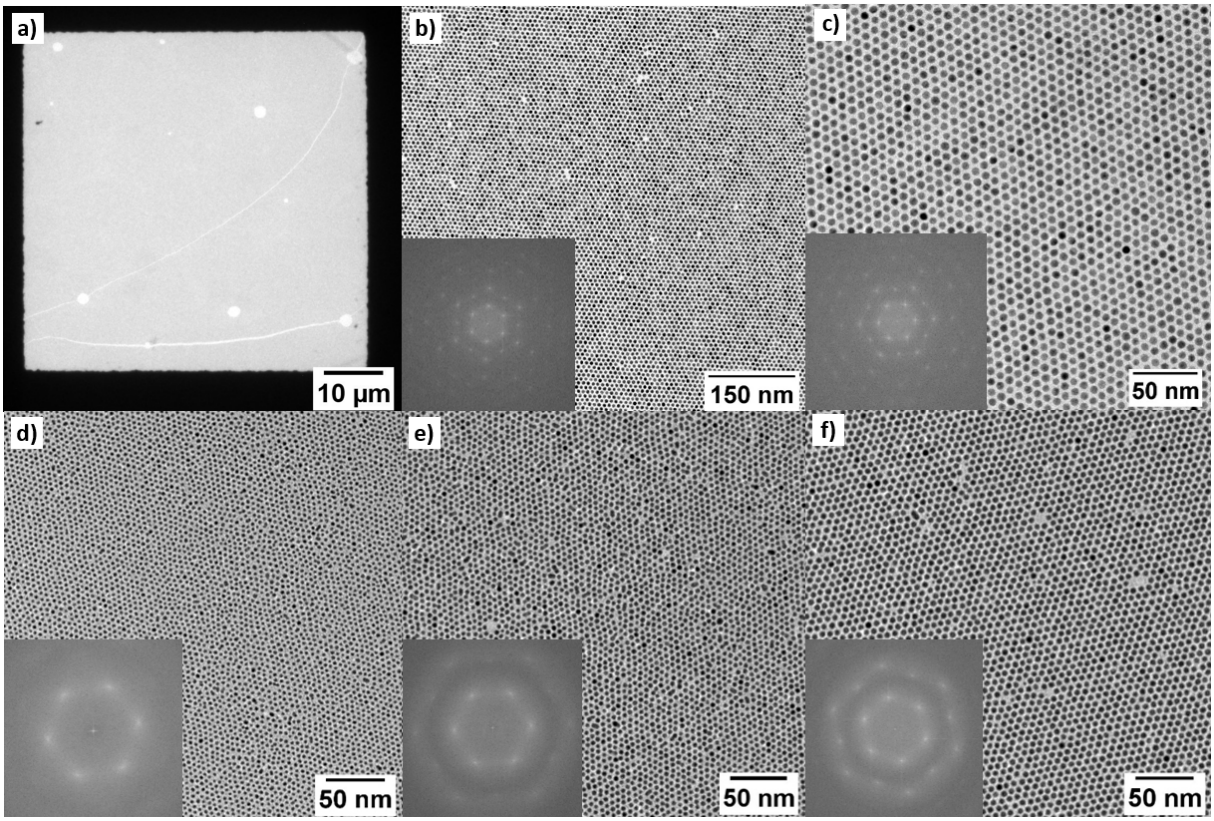

Fig. 2. TEM images of self-assembled Au NPs with different sizes. a) Low resolution TEM image showing the homogeneity of the film composed of 6.4 nm Au NPs over very long distances (around 50 μm). b) and c) Hexagonal lattice of 6.4 nm gold NPs. TEM images of self-assembled Au NPs of (d) 3 nm, (e) 4 nm, and (f) 5.1 nm.

In our series of staggered sized NPs, the 6 nm NPs batch was initially an outlier in this trend of increased order of increased size. These NPs yield homogeneous and extended monolayers but surprisingly they did not display a long-ranged hexagonal symmetry as observed for smaller and larger NPs (Fig. 3a). The film displayed many lacunae and empty spherical or oval-shaped areas with diameters ranging from 2 to 10 μm (see Fig. S12). In some parts of the monolayers, there were small areas of a few μm^2 of bilayers without long-range order.

We hypothesized that this might be due to a smaller density of ligands at the surface of the NPs caused by the washing step after synthesis. We thus added hexadecanethiol at different concentrations in the solution after the washing and before the self-assembly. We found that adding a minimum of 1.72×10^{-5} mol/L thiols in solution prior to self-assembly enabled the recovery of the long ranged organization obtained for the other particles (Fig. 3b).

Several different effects could explain this observation. A recent paper by the Tisdale group (42) showed that unbound ligand in solution had a pivotal role on the superlattice structure obtained by evaporating PbS nanocrystal dispersion. In this case, molecular dynamics simulations showed that even if the ligand does not bound to the surface, it swells the nanoparticle ligand shell which makes the interaction between particles softer. Apart from this influence on interparticle forces, free ligand in solution can also impact the dynamics of the evaporation and hence the self-assembly kinetics. As a surfactant, hexadecanethiol will adsorb at the liquid-air interface to reduce its interfacial tension and change the evaporation rate in a non trivial fashion (43). More controlled experiments would be required to favor one of these scenarios.

Then, we studied the self-assembly of PSSH coated 9.4 nm NPs. We observed extended films over distances that span tens of micrometers (Fig. S13) displaying well-ordered hexagonal superlattices, in which the average NP edge-to-edge distance is (2.5 $\pm$ 0.3) nm. The extended length of PSSH being around 3 nm (4), the ligands are highly interdigitated. However these films are not totally homogeneous and we also observed alongside well organized superlattices, parts of the TEM grid where fused NPs are present (Fig. S13). This might be due to an incomplete ligand exchange between CTAC and PSSH, as pointed out by Schulz *et al.* (39), which induced the fusing of NPs in solution and prevents the formation of long-ranged hexagonal monolayers. This is also consistent with our observation that these dispersions are not colloidally stable in the long term.

Going further in the size increase, we performed the self-assembly of gold NPs with average core diameter of 11.3 and 14 nm under the same experimental conditions (Fig. 4). These NPs are faceted and display a variety of shapes: spheres, tetrahedrons or more irregular shapes. However, they display highly organized films displaying hexagonal symmetry with areas reaching 10^3 μm^2 for 14 nm Au NPs

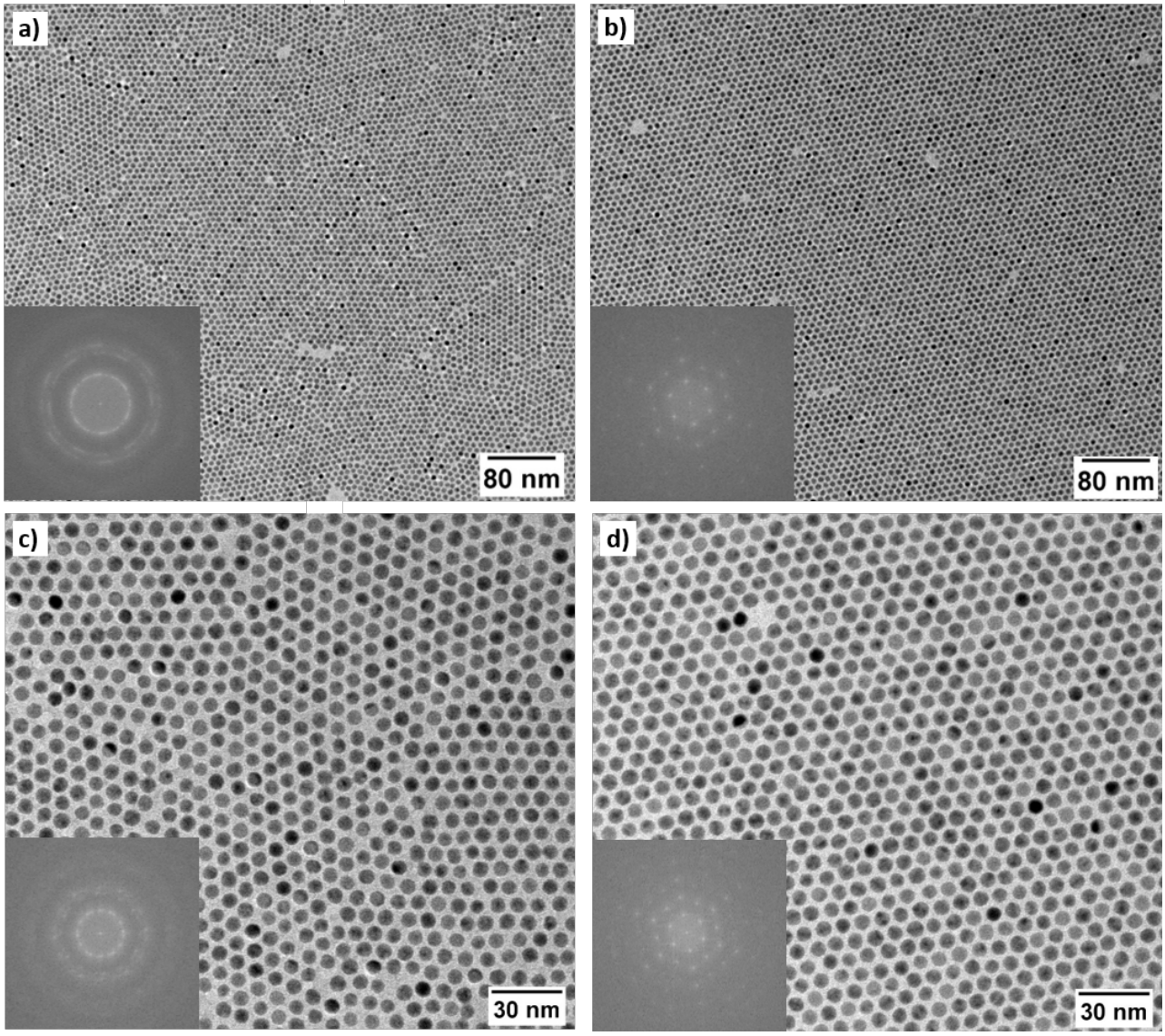

Fig. 3. Effect of added thiol in solution for 6 nm nanoparticles: a) and c) short range ordered films without thiols, b) and d) long ranged ordered films with thiols.

coated by OLA (Fig. S14) and less than 0.1% of lacunae.

Interestingly, for these larger NPs (11.3 and 14 nm of diameter), coated by OLA or PSSH, long-ranged and well-ordered hexagonal superlattices were obtained even if the NPs have a high shape polydispersity (Fig. 4). These large ligands can compensate the NP dispersion in size and shape. The soft corona helps the NPs organize in a more compact arrangement, regardless of the core shape. In the case of larger particles and in contrast with what was found before with particles in the 3 to 6 nm range, monodispersity is not essential to form superlattices with long range order.

For hexadecanethiol coated nanoparticles, we noticed that the edge-to-edge interparticle distance in the hexagonal lattice slowly increases with size, going from (1.2 ± 0.2) nm for the 3 nm to (1.3 ± 0.2) nm for the 4 nm, (1.6 ± 0.2) nm for the 5 nm and (1.7 ± 0.2) nm for the 6.4 nm Au NPs. There is in all cases a significant interpenetration of the carbon chains between adjacent NPs since the extended length of hexadecanethiol is around 2.2 nm (29). This increased spacing between the NPs was also observed in assemblies in solution for the same kind of NPs dispersed in decane with core diameters smaller than 8 nm (29). For larger particles, the ligands also interdigitate with, for example, an edge-to-edge distance of (3.8 $\pm$ 0.3) nm for PSSH coated 11 nm Au NP to be compared to 6 nm for twice the ligand length.

Interestingly, the solvent also impacts the edge-to-edge distance. 5.0 nm Au NPs coated by 1-dodecanethiol and dispersed in hexane yield extended monolayers with hexagonal symmetry (Fig. S15) with large-areas of long range NPs (around 5 μm^2). Within the hexagonal monolayers the ligands are highly interdigitated with a mean edge-to-edge distance of (1.9 $\pm$ 0.3) nm, much smaller than the two fully extended dodecane chains (2 $\times$ 1.7 nm). This distance is larger than for hexadecanthiol coated NPs where the ligands are longer. We believe this could be due to the stronger tendency of toluene to penetrate into the monolayers than

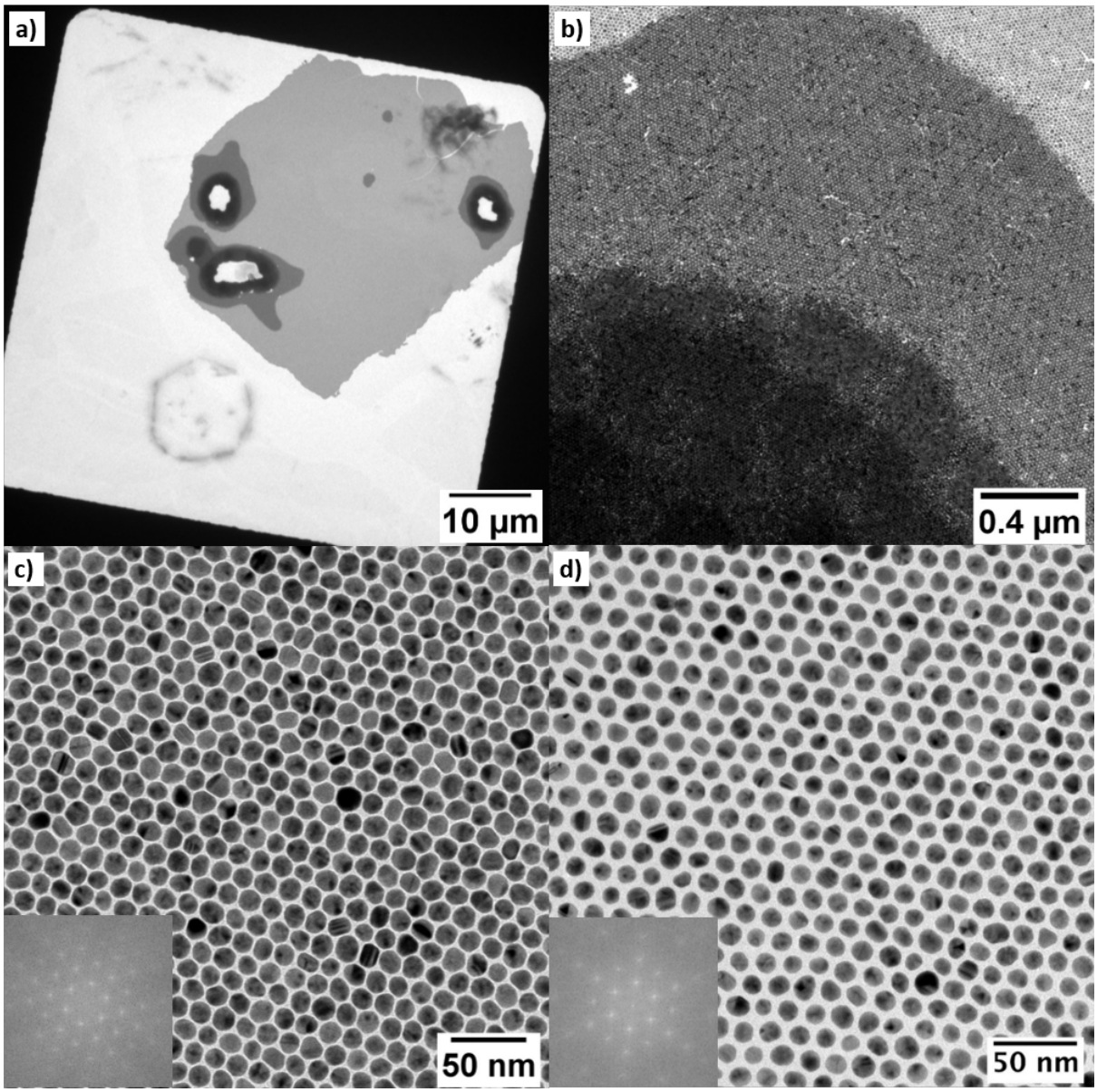

Fig. 4. a-c) TEM images of self-assembled 14 nm Au NPs. Low magnification of a film composed in majority of monolayers (light area) and of bi- and multilayers (darkest areas) (a). Transition from a monolayer to multilayers (b). Hexagonal monolayers of 14 nm NPs coated with OLA (c) and 11.3 nm NPs coated with PSSH (d).

hexane. Interestingly, we also noted in this case a size segregation phenomenon since polydispersity is lower in the self-assembled monolayers than in solution (Fig. S15).

In order to rationalize our results, we compared our experimental data for the inter particle distances within the films with two models predicting the equilibrium distance between NPs in assemblies depending on the ratio between the fully extended chain length and the NP radius (Fig. 5). Both model's constituting equations relate the volume available to the ligand in a given lattice to the one required by geometrical constraints which depend on the density of ligand, their chain length and the radius of the NPs. In the Optimal Packing Model (OPM) (31) the ligands at the surface pack with the same density as a fully elongated chain. In this case, the ligands do not interpenetrate and the cones which delimits the available space for ligands on two separate particles do not overlap. This model was found to describe well experimental data for PbS and Au NPs of 3-5 nm core diameter with ligand containing 9 to 18 carbons. (44) In contrast, the Overlap Cone Model (OCM) (33) considers an intersection of ligands cone belonging to neighboring NPs. By doing so, multi-body effects can be taken into account and ligands of different NPs in the lattice are allowed to interpenetrate. Both models predict the parameter $\tau = r/R$, where r is the effective radius of the particles within the assembly (i.e. the radius of the core plus the actual length of the ligand) and R is the radius of the core, as a function of $\lambda = L/R$, where L is the maximum extension of the ligand. In both cases, one has to assume a value for the normalized molecular area of the ligand on the surface $\xi = \sigma/\sigma_m$, where σ and σ_m are the actual and maximum ligand grafting density. In the following, we hypothesized a full coverage, i.e.

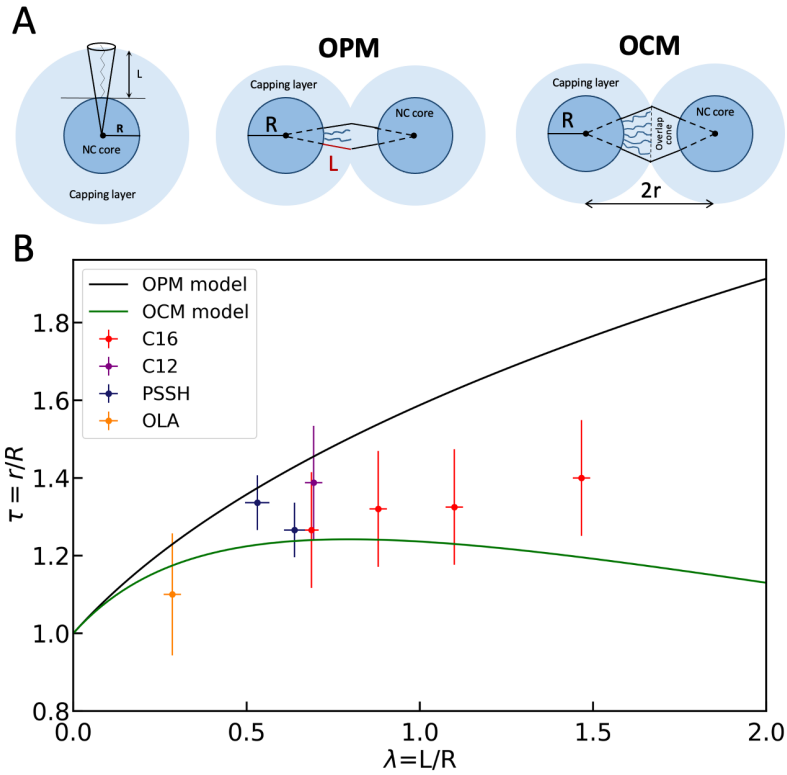

Fig. 5. A) Description of the OPM and OCM models with the relevant notations. B) Comparison of the OCM and OPM models relating the τ and λ parameters with the experimental results for gold NP monolayers with different ligands: hexadecanethiol (C16), dodecanethiol (C12), thiolated polystyrene (PSSH) and oleylamine (OLA).

xi=1 and discuss this assumption afterwards.

We plotted τ as a function of λ to compare their value for the different experimental conditions to the ones predicted by the OPM and OCM models (Fig. 5B). We see that neither of the two models reproduces all our data well. The OPM model overestimates the equilibrium distance for all λ values while the OCM model underestimates λ for all experimental points except the oleylamine case. Our results are consistent with MD simulations (45) where all points with λ parameters larger than 0.5 fell between the OCM and OPM model while for smaller values the OCM model yielded an overestimation of τ. We analyzed the sensitivity of these results to our hypothesis of full chain grafting since a lower chain density would result in $\xi < 1$. To do so, we plotted our experimental results along a series of OCM-OPM theoretical curves with values of σ ranging from 0.6 to 1 (Fig. S16). For the OCM model, decreasing the ξ parameter does not result in a better agreement with our data. Taking into account lower surface graftings makes the OPM model closer to the experimental points but with significant deviations for large λ values even at very low surface grafting densities. Besides purely geometrical effects taken into account in these models, other effects can influence the mean distance between the particles. The van der Waals attraction between the cores increases with size but this would lead to a decrease of the interparticle distance since the ligand shell will be more compressed for stronger attraction between the cores. But the ligand-ligand entropic interactions is also impacted by the NP size. When the size of the NPs increases, the curvature of the interface decreases and the alkyl chains have less and less space to explore different configurations. A larger ligand density thus induces an increase in the mean edge-to-edge length which would ultimately reach twice the length of the ligand shell for flat 2D NPs (29). Overall, this experiments / theory comparison shows that the OPM and OCM models do not capture well our experimental findings and shows that further theoretical refinements are needed.

We now consider the effect of aging of the colloidal dispersion on their self-assembly. We noticed that when the NPs were stored dried and redispersed just prior self-assembly, the results were highly reproducible. In contrast, when they were kept dispersed in a solvent under ambient conditions the NPs fused. For example, from the self-assembly of a batch of gold NPs stored for six months in hexane, we observed the formation of superlattices composed of sintered NPs that form a semi-continuous network which has a hexagonal symmetry (Fig. S17). We hypothesized that during storage in a solvent, the alkanethiols initially bonded to the surface desorb which decreases the ligand surface density (46). When assembled on a surface, the lower ligand coverage induces fusion between adjacent NPs to minimize the surface energy during the self-assembly. This aging effect was already reported for Au NPs coated by decanethiol and dispersed in toluene and self-assembled in binary mixtures (47).

Though the films are mostly composed of a single layer of NPs, multilayers are also present. We can clearly distinguish the number of monolayers with a smooth transition from a

single layer, to two, three and more layers. These few layers films are less extended than the monolayer but all have hexagonal symmetry. They can be seen as precursors of 3D crystals and thus give hint on the first steps of crystallisation. We can distinguish 2 types of structures which are particularly interesting: a $CaCu_5$ phase, which is supposed to be a binary phase but obtained in our case from a monodisperse population with size segregation and Moiré patterns which result from the twisted superposition of two (or more) monolayers. We detail these two original structures in the following.

For 11.3 nm Au NPs coated by PSSH, we observe not only the formation of hexagonal monolayers, but also structures where two or three layers are superimposed with two types of arrangements. First, in several regions, two or three hexagonal layers are packed at the top of each other in a close packing fashion, with the occurrence of AB, ABA and ABC sequences (Fig. 6c). In such regions, the NPs have a very narrow size distribution (11.3 $\pm$ 1.2) nm. Second, we observe another periodic arrangement of NPs in adjacent regions to the close packed ones. Surprisingly, it contains two distinct sizes of NPs, "small" ones with of size (11.5 $\pm$ 1.1) nm and "large" ones of size (14.6 $\pm$ 1.1) nm. From the TEM images, we can analyze this structure in the following way. We identify a superposition of three layers (Fig. 6) that can be attributed to a $CaCu_5$ binary phase (space group P6/mmm), with the "small" NPs corresponding to the Cu sites and the "large" ones to the Ca sites (see Fig. 6a, b, f-h). The top and bottom layers are identical and contain both "small" and "large" NPs in a ratio 2:1 with an intermediate layer in-between containing only "small" NPs arranged on a Kagomé lattice (see Fig. 6h). A Kagomé lattice is a pattern composed of triangles and hexagons and is one of the eleven Archimedean tilings. Such $CaCu_5$ binary phase has been already reported in binary mixtures of metallic NPs, among other possible arrangements (44). The effective ratio between the small and the large NPs (γ ratio) reported in (44) is 0.76. We have calculated an average gamma of 0.83 ($\pm$ 0.3), which is slightly higher.

The observation of such a binary phase from a single population is remarkable because the starting size distribution is already narrow. The size of the "small" and "large" NPs at the two sites differ by more than 25% showing that the single population of NP can behave as a binary one with a size segregation occurring at different sites of a complex lattice. Interestingly, based on X-ray scattering analysis, a similar binary phase ($MgZn_2$, also called C14 Frank-Kasper) has been reported in the bulk for a single population of much smaller 2 nm gold NPs coated by hexanedecanethiol (15) and in aqueous dispersions of colloidal silica (24). Here, we observe directly the size segregation at the single particle level at different sites in the TEM images. Moreover, as only two or three layers are imaged, we are able to compare the structure of the $CaCu_5$ binary phase with nearby domains made of close packed arrangements of NPs with a single size. Finally, we can note that the $CaCu_5$ phase contains both Z20 and Z12 coordination sites. In this respect, it is not strictly a Frank-Kasper phase, that may contain only combinations of Z12, Z14, Z15 and Z16 coordination sites, but it is closely related.

Another type of bilayer structures observed in our samples are Moiré patterns. They result from the overlapping of two hexagonal closed-packed layers with some twist angle (α). Moiré patterns are attracting more and more attention motivated by the recent discoveries about twisted double layer graphene and in the new field of twistronics (48–50). In the case of colloidal NPs, there are several examples of Moiré patterns for metallic NPs like ruthenium nanospheres (51) and gold nanorods (52–54). These structures were observed from the self-assembly of NPs of different sizes and coated by different ligands (Fig.7 and S18-S19): 4.9 nm NPs coated by dodecanethiol (Fig. 7a), 6 nm NPs coated by hexadecanethiol (Fig. 7b), 12 nm NPs coated by OLA (Fig. 7c), and 11.3 nm NPs coated by PSSH (Fig. 7d). By comparing the structures observed in the TEM images with numerical simulations of two layers twisted with a known angle we could identify this angle. In Fig. 7, we show the models of Moiré patterns obtained by rotating the upper hexagonal layer with respect to lower one at different twist angles α.

In Fig. 7b and c, some areas show deviations from a Moiré pattern. This may be due to a different hexagonal order between the two layers which is locally modified by the directional NP interactions due to their faceting (55). This hypothesis explains the formation of these patterns, which are not predicted from the hard-sphere model. In Fig. 7d two hexagonal layers are overlapped at α = 30°. In this instance, the NPs arrangement have a quasicrystalline order with a 12-fold rotational symmetry. We have also observed the formation of Moiré patterns composed of more than two hexagonal layers. For example, Fig. S19 shows the formation of several Moiré structures from the overlapping of more than two layers. Viau *et al.* found that the formation of Moiré patterns from the self-assembly of spherical 4 nm ruthenium NPs was favored by a high evaporation rate and a low ligand concentration (51). They hypothesized that the NPs may be stacked in a non-equilibrium state which produces this kind of patterns.

It is interesting to underline that the behavior of the NPs coated with PSSH with two different sizes (9.4 nm and 11.3 nm) is quite different when a few layers are superimposed. For the smallest size (9.4 nm), there is a predominance of Moiré patterns with variable Moiré twist angles. There is thus no strong coupling from one layer to the next one as no strong correlation in orientation between them is present. In contrast, for the largest size (11.3 nm), the layers are strongly coupled to each other with the emergence of 3D periodic structures: either close-packed structures or a binary phase ($CaCu_5$). Hence, for the PSSH ligand, a critical size for the gold core (around 10 nm) is evidenced between a stack of essentially independent 2D layers (Moiré patterns) to a 3D behavior with the genesis of periodic superlattices.

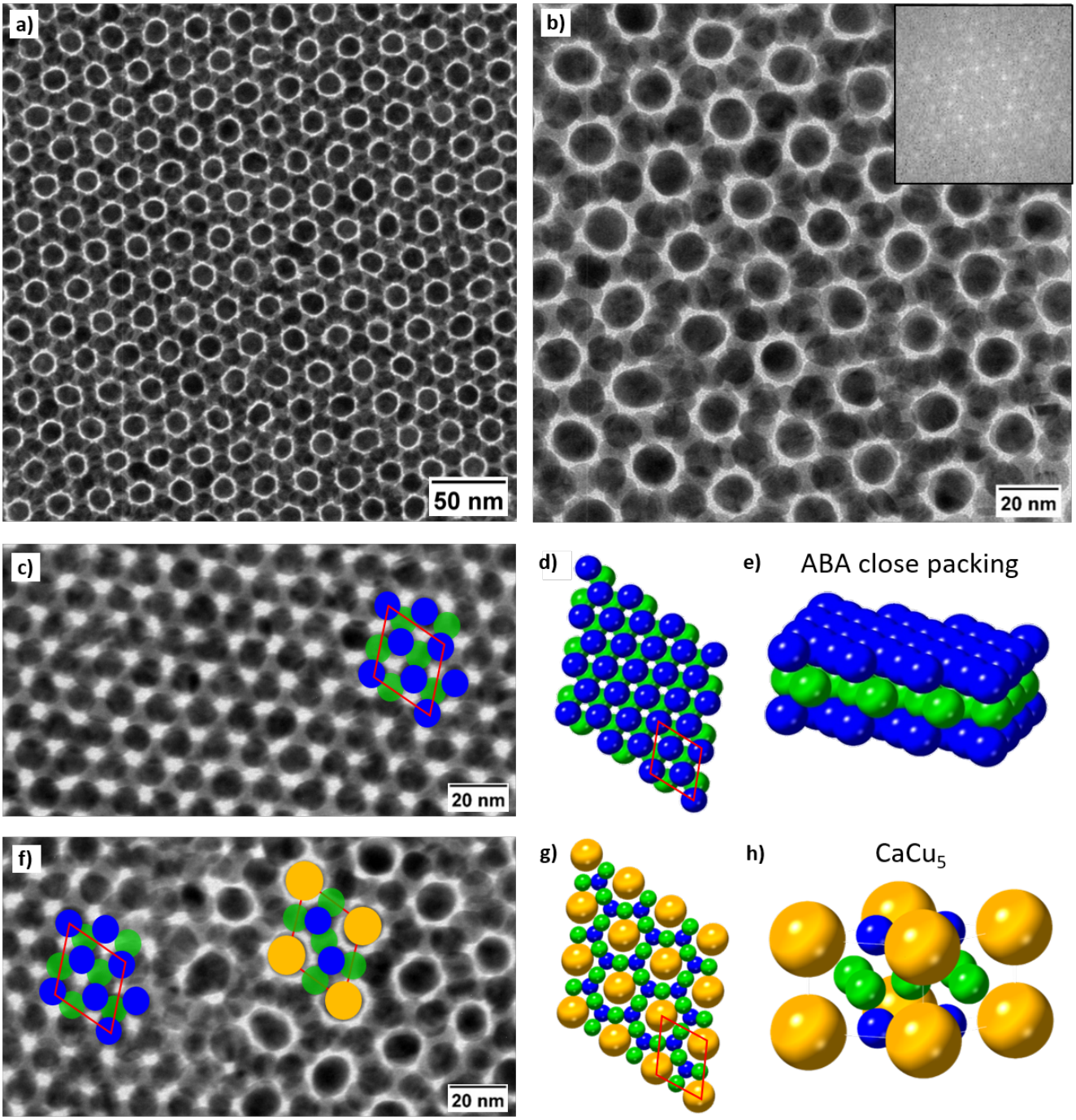

Fig. 6. TEM images and models of self-assembled 11.3 nm Au NPs coated by PSSH. a) and b) Binary hexagonal $CaCu_5$ phase (P6/mmm group), the inset shows the Fourier transformed image. c) Three hexagonal layers of "small" NPs packed in a ABA sequence, d) 2D and e) 3D models. f) TEM image showing the insertion of the "large" NPs into the ABA packing structure. g) 2D and h) 3D models of the binary $CaCu_5$ phase.

Conclusion

We have investigated the 2D self-assembly of spherical Au NP with sizes ranging from 2 to 14 nm coated by different ligands, from the evaporation of a dispersion on a liquid surface. We have explored different experimental conditions to obtain well-ordered superlattices in a robust and reproducible fashion. We observed the formation of long-ranged superlattices for diameters between 2 and 6 nm, but only NPs larger than 3 nm arrange in regular close-packed hexagonal monolayers extending over a few microns in size. The hexagonal order in the close-packed layers improves by increasing the size of the NPs. We have also shown that their organization in hexagonal close-packed layers was favored by dispersing them in toluene (rather than in hexane or cyclohexane) and by the addition of free thiol in solution prior to self-assembly. The comparison between experimental inter-particle distances within the film with widely used geometrical OPM and OCM models shows that supplementary ingredients are needed for further model refinement.

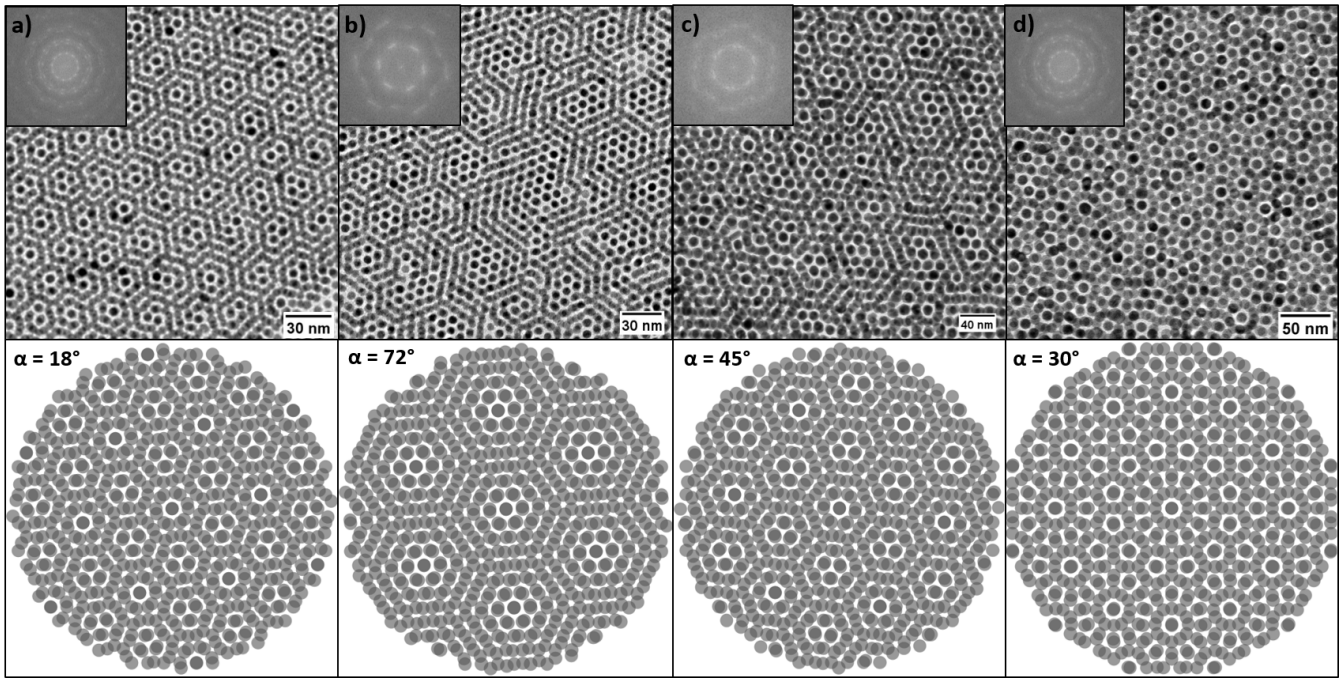

Fig. 7. TEM images of different Au NPs assembled in Moiré patterns from the overlap of two hexagonal layers with different twist angles (α). a) 4.9 nm NPs coated by dodecanethiol with a α of 15°. b) 6 nm NPs coated by hexadecanethiol with a α of 72°. c) 12 nm NPs coated by OLA with a α of 45°. d) 11.3 nm NPs coated by PSSH with a α of 30° having a 12-fold rotational symmetry.

These insights on a model system can be extended to other types of nanoparticles with more complex shapes. We have reported the discovery of a binary $CaCu_5$ phase from the self-assembly of a single population of 11.3 nm Au NPs coated by thiolated-polystyrene ligands. The observation of a binary phase for a single population is a surprising finding. A size segregation between "large" and "small" NPs is directly observed on the TEM images. This binary phase is attributed to a co-crystallization phenomenon coupled with segregation in size. This might explain the genesis of some other complex phases such as Frank-Kasper phases, to which the $CaCu_5$ phase is closely related. In addition, Moiré patterns resulting from the superposition of hexagonal close-packed layers are observed. Several twist angles from one layer to the other are observed within the same sample, showing a weak coupling between the two layers. However, one system (11.3 nm NPs coated by PSSH) shows a Moiré pattern with the predominance of 30° angle which corresponds to a 12-fold quasicrystalline order. Alternatively, a more standard close-packing of a few hexagonal layers is obtained. These results open the way to a possible route using self-assembly to control the angle of a Moiré pattern, a current hot topic for NP superlattices (53, 56). Our work might be interesting for further investigation on the self-assembly of binary NP superlattices. Fascinating optical properties might also emerge from these assemblies.

Experimental Section

A. Chemicals. All chemicals were used as received without further purification. Hydrogen tetrachloroaurate(III) hydrate ($HAuCl_4 \cdot H_2O$, 99.8%) and chlorotriphenylphosphinegold(I) ($AuCl(PPh_3)$, 98%) were purchased from Strem Chemicals. Hexadecanethiol (95%), tetraoctylammonium bromide (98%, TOAB), borane tert-butylamine complex (97%, TBAB) and sodium borohydride (96%) were purchased from Merck. Diethylene glycol (DEG, 99%), hydrogen tetrachloroaurate ($HAuCl_4 \cdot 3H_2O$, 99.99%) and tetrabutylammonium borohydride (TBAB, 98%) were purchased from Alfa Aesar. 1-dodecanethiol (98%), cetyltrimethylammonium bromide (CTAB), ascorbic acid (AA) and citric acid monohydrate ($\geq$ 99.5%) were purchased from Sigma Aldrich. Cetyltrimethylammonium chloride (CTAC) was purchased from Acros Organics. Oleylamine (approximate C18-content 80-90%, OLA), toluene (99%), cyclohexane, n-hexane ($\geq$ 95%), acetone, ethanol (96%) and isopropanol were purchased from Fisher Scientific. Sodium citrate dihydrate (99%) and 1,2,3,4- tetrahydronaphthalene (tetralin) were purchased from Fluka. ω-thiol-terminated polystyrene (PSSH of 2kDa) was purchased from Polymer Source.

B. Synthesis of gold nanoparticles. NPs with a diameter between 2 and 5 nm coated with hexadecanethiol were synthesized by following a seeded growth protocol as described by Goldmann *et al.* (34)

6 nm NPs were made by following the Stucky method (36). 200 mg of $AuCl(PPh_3)$ were dispersed in 40 mL of toluene with 800 μL of hexadecanethiol. 355 mg of TBAB were dissolved in 24 mL of toluene. The two solutions were heated separately at 100°C for 2 minutes and then the TBAB solution was rapidly added to the other one. At the end of the addition, the heating was continued for 2 minutes and the particles were cooled back to room temperature, precipitated

with ethanol, filtered (by using a 0.2 μm PTFE syringe), washed firstly with ethanol, then with acetone. Finally, the dark brown precipitate was dried.

4.9 nm Au NPs coated by 1-dodecanethiol were synthesized by following the protocol described by Cargnello *et al.* (19) *tert*-butylamine-borane complex (88 mg, 1 mmol) was dissolved by sonication in 2 mL OLA and 2 mL tetralin and rapidly injected into a solution of $HAuCl_4 \cdot 3H_2O$ (196 mg) in 20 mL OLA and 20 mL tetralin at room temperature in a 50 mL three-necked flask. The Au reduction had occurred almost immediately, as shown by a change in colour from orange to dark red, but the reaction was left stirring in air for 1 h. The flask was then sealed and flushed with Ar, and the temperature was increased to 60°C using a heating mantle. At this stage, 100 μL 1-dodecanethiol were mixed with 0.9 mL OLA, and this solution was slowly added using a syringe. At the end of the addition (after about 3 min), the flask was cooled and opened to the air. NPs were then purified three times by precipitating them in a mixture solvent of isopropanol/ethanol (3/1, 40 mL), centrifuging (8000 rpm, 3 min), and dissolving them in hexane (10 mL). Finally, the Au NPs were dried in a desiccator and redispersed in hexane.

5.9 nm NPs coated by OLA were synthesized by following the protocol reported by Peng *et al.* (37). $HAuCl_4 \cdot 3H_2O$ (102.7 mg) was dissolved in a solution of tetralin (10 mL) and OLA (10 mL) in air at 4°C using an ice-water bath in a 50 mL three-neck flask and magnetically stirred under Ar flow for 10 min. The reducing agent *tert*-butylamine-borane complex (0.5 mmol, 43.2 mg) was mixed with tetralin (1 mL) and OLA (1 mL) by sonication, and then injected into the orange precursor solution with a syringe. The reduction was instantaneously initiated and the solution changed to a deep red color immediately. The mixture was allowed to react at 4°C for 1 h before acetone (60 mL) was added to precipitate the Au NPs. They were not collected after three centrifugations (8500 rpm, 8 min and 20 min). Other 80 mL of acetone were added to the mixture, and after two further centrifugations (8500 rpm, 8 min) the Au NPs were collected and washed with acetone. The vials were left drying in a desiccator and 103.2 mg of purified product were recovere. The NPs were redispersed in hexane.

NPs with diameters around 9 nm were synthesized following the scaled-up synthesis reported by Zheng *et al.* (38) A fresh aqueous $NaBH_4$ solution (10 mM, 0.6 mL) was rapidly added into a mixed 10 mL aqueous solution containing $HAuCl_4$ (0.25 mM) and CTAB (100 mM). A brown solution immediately formed upon the introduction of $NaBH_4$. The mixture was placed under stirring at 300 rpm for 3 min, and then kept undisturbed at 27°C for 3 h to ensure complete decomposition of $NaBH_4$ remaining in the reaction mixture. Aqueous solutions of CTAC (200 mM, 20 mL), AA (100 mM, 15 mL), and the initial CTAB-capped Au clusters (0.5 mL) were mixed in a 125 mL glass bottle, followed by one-shot injection of 350 μL of an aqueous $HAuCl_4$ solution (0.5 mM, 20 mL). The reaction was allowed to continue at 27°C for 15 min. The product was collected by centrifugation at 20000 rpm for 20 min, and then dispersed in 10 mL of aqueous CTAC solution (20 mM).

NPs with diameters between 11.3 and 14 nm were synthesized following a modified Turkevich protocol by using a citrate buffer solution as the reducing agent and stabilizer. Then, these citrate-coated NPs were transferred to toluene by a ligand exchange with OLA or PSSH. To obtain gold NPs of 12 nm the protocol described by Schulz *et al.* was followed (40). 125 mg of sodium citrate dihydrate and 29 mg of citric acid monohydrate were dissolved in 200 mL of distilled water. A volume of 200 mL of 2.75 mM citrate buffer (75/25 sodium citrate/citric acid monohydrate) in a 400 mL beaker was heated to its boiling point on a hot plate with a magnetic stirrer. The beaker was covered to minimize evaporation of water. Meanwhile, 50 mL of an aqueous $HAuCl_4 \cdot H_2O$ solution (c = 812.5 μM) was heated to 90-100°C to prevent a decrease in temperature during subsequent mixing. The citrate buffer was kept at the boiling point for 15 min and then the Au precursor solution was quickly added while the mixture was being stirred (200 rpm, 50 mm x 8 mm cylindrical stirring bar). After the color of the solution had changed (violet, purple, pink and finally red), it was heated at the boiling point for an additional 20 min before the hot plate was switched off to let the solution cool to room temperature. The solution was then transferred into a glass bottle for storage.

C. Ligand exchange. We followed the protocol reported by Schulz *et al.* (4) Citrate-coated gold NPs were used as synthesized. Oleylamine (0.4 mM) or PSSH (0.16 mM) in toluene were mixed with aqueous Au NPs coated by citrate and ethanol in a ratio of 1:1:1. The solution was thoroughly mixed in a closed flask until a homogeneous pink solution had formed. The reaction was allowed to take place overnight at room temperature under stirring before the organic phase was carefully extracted. The NPs coated by OLA were purified by syringe filtration (with a PTFE of 0.2 μm), meanwhile the Au NPs coated by PSSH were purified by two centrifugation steps (10 min, 20000 g) and then redispersed in toluene.

D. Self-assembly at liquid-air interface. Self-assembly experiments were carried out using a drying-mediated method (11). A Teflon well with a cylindrical hole (diameter and height of 1 cm) filled with 0.3 mL of DEG was used as support. Depending on the NP concentration a given amount of Au NPs dispersion, prepared by dissolving the as-synthesized NPs in toluene (with a NP concentration of around 20 nM), were drop cast on the DEG surface in a Teflon well, which was then covered with a glass slide to slow down the evaporation process. To determine the volume of gold NP dispersion to deposit, we estimate (depending on their size and ligand chain length) the number of NPs needed to cover all the DEG surface with a single layer by considering the maximal packing density of discs in a plane (0.9069). For example, for 6 nm coated with hexadecanethiol ligands,

this corresponds to 1.40×10^{12} particles. The concentration in NP of the dispersion is measured by UV/VIS spectroscopy with molar extinction coefficients taken from Haiss *et al.* (57). The volume added is then adapted to reach the desired number of NPs. For example, for a dispersion of 2 mg/mL in gold after synthesis and purification, this corresponds to a volume of around 60 μL of a 50 fold dilution. After deposition, the solvent was allowed to evaporate and a solid film formed after complete evaporation. We regularly observed the formation of pink films on the DEG surface which have a mirror character, as shown in Fig. 1d. The NP film is carefully recovered by placing a TEM grid (held by a pair of tweezers) under the floating film and then gently lifted upwards to collect it. The substrates were then dried in a desiccator to remove residual DEG for at least 24 hours.

E. SAXS characterization. SAXS measurements were performed using a home-made MODIX instrument (LPS, Orsay). A rotating anode X-ray generator (40 kV, 40 mA) is equipped with a molybdenum target (wavelength Mo K_α=0.71 Å, energy 17 keV) and a collimating multilayer X-ray optic (Max-Flux optic, RIGAKU). Samples were prepared in glass capillaries (diameter 2 mm) filled with a 1 wt% solution of NPs in toluene and placed on the motorized sample holder of the instrument. 2D SAXS images were acquired on a two-dimensional image-plate detector (MAR 345 mm). Data reduction to the radially averaged intensity I(q) was done using the NIKA macros written for IgorPro (Wavemetrics, Oswego, USA)(58). The sample to detector distance of 760 mm was calibrated using a quartz powder. The range of scattering vectors q was between 0.05 Å and 3.1 $Å^{-1}$. The SAXS intensity curves I(q) were fitted with SasView software using a polydisperse sphere model with a Schultz-Zimm distribution. SAXS measurements were also performed using XENOCS XEUSS 3.0 instrument using glass capillaries of 1 mm. The SAXS intensity curves I(q) were fitted with XSACT software.

F. Electron microscopy and image treatment. TEM images of the superlattices were obtained by using a JEOL JEM2100 equipped with a LaB_6 thermionic electron gun and a High Tilt objective pole piece. The microscope was operated at 200 kV with a point-to-point resolution of 0.25 nm. Measurements of the particle organization, the interparticle distances, and the amount of lacunae were done by using the open-source ImageJ software. We have performed this count on at least 1000 NPs.

The amount of lacunar defects was calculated from the number of nanoparticles measured in a 0.5 μm^2 region of the hexagonal monolayer (more than 10000 NPs). We then calculated the number of NPs to cover the same area without any lacunae and divided the two numbers (Fig. S20).

G. UV/Vis Spectroscopy. Absorbance measurements were recorded with a Perkin Elmer UV-vis-NIR Lambda 750 spectrophotometer. The Au NP concentrations in toluene were calculated by measuring their absorbance at 450 nm, by using the molar extinction coefficients reported in (57).

ACKNOWLEDGEMENTS

This work is funded by the ANR grant ANR18-CE09-0025 (Project SoftQC). This work was supported by the LABEX iMUST of the University of Lyon (ANR-10-LABX-0064), created within the "Plan France 2030" set up by the french government and managed by the French National Research Agency (ANR). We thank Nicholas Blanchard and ILMTech for acces to JEOL 2100 TEM. We thank Alex Travesset and Mathieu Kociak for stimulating discussions.

1. Sharon C Glotzer, Michael J Solomon, and Nicholas A Kotov. Self-assembly: From nanoscale to microscale colloids. *AIChE J.*, 50:2978–2985, 2004.
2. Margaret S Lee, Daryl W Yee, Matthew Ye, and Robert J Macfarlane. Nanoparticle assembly as a materials development tool. *Journal of the American Chemical Society*, 144(8):3330–3346, 2022.
3. Michael A Boles, Michael Engel, and Dmitri V Talapin. Self-assembly of colloidal nanocrystals: From intricate structures to functional materials. *Chemical reviews*, 116(18):11220–11289, 2016.
4. Florian Schulz, Steffen Tober, and Holger Lange. Size-dependent phase transfer functionalization of gold nanoparticles to promote well-ordered self-assembly. *Langmuir*, 33(50): 14437–14444, 2017.
5. Yang Liu, Marco Klement, Yi Wang, Yaxu Zhong, Baixu Zhu, Jun Chen, Michael Engel, and Xingchen Ye. Macromolecular ligand engineering for programmable nanoprism assembly. *Journal of the American Chemical Society*, 143(39):16163–16172, 2021.
6. Jessica Cimada daSilva, Daniel M Balazs, Tyler A Dunbar, and Tobias Hanrath. Fundamental processes and practical considerations of lead chalcogenide mesocrystals formed via self-assembly and directed attachment of nanocrystals at a fluid interface. *Chemistry of Materials*, 2021.
7. J Mohapatra, J Elkins, M Xing, D Guragain, Sanjay R Mishra, and J Ping Liu. Magnetic-field-induced self-assembly of feco/cofe$_2$o$_4$ core/shell nanoparticles with tunable collective magnetic properties. *Nanoscale*, 13(8):4519–4529, 2021.
8. CB Murray, CR Kagan, and MG Bawendi. Self-organization of cdse nanocrystallites into three-dimensional quantum dot superlattices. *Science*, 270(5240):1335–1338, 1995.
9. Elena V Shevchenko, Dmitri V Talapin, Nicholas A Kotov, Stephen O'Brien, and Christopher B Murray. Structural diversity in binary nanoparticle superlattices. *Nature*, 439(7072): 55–59, 2006.
10. Maryna I Bodnarchuk, Maksym V Kovalenko, Wolfgang Heiss, and Dmitri V Talapin. Energetic and entropic contributions to self-assembly of binary nanocrystal superlattices: temperature as the structure-directing factor. *Journal of the American Chemical Society*, 132 (34):11967–11977, 2010.
11. Angang Dong, Jun Chen, Patrick M Vora, James M Kikkawa, and Christopher B Murray. Binary nanocrystal superlattice membranes self-assembled at the liquid–air interface. *Nature*, 466(7305):474, 2010.
12. Niclas S Mueller, Yu Okamura, Bruno GM Vieira, Sabrina Juergensen, Holger Lange, Eduardo B Barros, Florian Schulz, and Stephanie Reich. Deep strong light–matter coupling in plasmonic nanoparticle crystals. *Nature*, 583(7818):780–784, 2020.
13. Christopher B Murray, Cherie R Kagan, and Moungi G Bawendi. Synthesis and characterization of monodisperse nanocrystals and close-packed nanocrystal assemblies. *Annual review of materials science*, 30(1):545–610, 2000.
14. Sang-Kee Eah. A very large two-dimensional superlattice domain of monodisperse gold nanoparticles by self-assembly. *Journal of Materials Chemistry*, 21(42):16866–16868, 2011.
15. S. Hajiw, B. Pansu, and J.-F. Sadoc. Evidence for a c14 frank–kasper phase in one-size gold nanoparticle superlattices. *ACS nano*, 9(8):8116–8121, 2015.
16. Daniel Huang, Frank Liao, Steven Molesa, David Redinger, and Vivek Subramanian. Plastic-compatible low resistance printable gold nanoparticle conductors for flexible electronics. *Journal of the electrochemical society*, 150(7):G412, 2003.
17. KC Chan, PF Lee, and JY Dai. Study of tunneling mechanism of au nanocrystals in hfalo matrix as floating gate memory. *Applied Physics Letters*, 92(22):223105, 2008.
18. Chi-Fan Chen, Shien-Der Tzeng, Hung-Ying Chen, Kuan-Jiuh Lin, and Shangjr Gwo. Tunable plasmonic response from alkanethiolate-stabilized gold nanoparticle superlattices: evidence of near-field coupling. *Journal of the American Chemical Society*, 130(3):824–826, 2008.
19. Matteo Cargnello, Aaron C Johnston-Peck, Benjamin T Diroll, Eric Wong, Bianca Datta, Divij Damodhar, Vicky VT Doan-Nguyen, Andrew A Herzing, Cherie R Kagan, and Christopher B Murray. Substitutional doping in nanocrystal superlattices. *Nature*, 524(7566):450, 2015.
20. Jaewon Lee, Elias Nakouzi, Miao Song, Bin Wang, Jaehun Chun, and Dongsheng Li. Mechanistic understanding of the growth kinetics and dynamics of nanoparticle superlattices by coupling interparticle forces from real-time measurements. *ACS nano*, 12(12):12778–12787, 2018.
21. J. L. Barrat and J. P. Hansen. On the stability of polydisperse colloidal crystals. *Journal de Physique*, 47(9):1547–1553, September 1986. doi: 10.1051/jphys:01986004709015400.
22. P. N. Pusey. The effect of polydispersity on the crystallization of hard spherical colloids. *Journal de Physique*, 48(5):709–712, May 1987. doi: 10.1051/jphys:01987004805070900.
23. P. N. Pusey, E. Zaccarelli, C. Valeriani, E. Sanz, Wilson C. K. Poon, and Michael E. Cates. Hard spheres: crystallization and glass formation. *Philosophical Transactions of the Royal Society A: Mathematical, Physical and Engineering Sciences*, 367:4993–5011, December 2009. doi: 10.1098/rsta.2009.0181. Publisher: The Royal Society Publishing.
24. Bernard Cabane, Joaquim Li, Franck Artzner, Robert Botet, Christophe Labbez, Guillaume Bareigts, Michael Sztucki, and Lucas Goehring. Hiding in Plain View: Colloidal Self-Assembly from Polydisperse Populations. *Physical Review Letters*, 116(20):208001, May 2016. doi: 10.1103/PhysRevLett.116.208001.
25. Carlos A. Silvera Batista, Ronald G. Larson, and Nicholas A. Kotov. Nonadditivity of nanoparticle interactions. *Science*, 350(6257):1242477, September 2015. ISSN 0036-8075, 1095-9203. doi: 10.1126/science.1242477.
26. Jason J Calvin, Amanda S Brewer, and A Paul Alivisatos. The role of organic ligand shell structures in colloidal nanocrystal synthesis. *Nature Synthesis*, pages 1–11, 2022.
27. Debora Monego, Thomas Kister, Nicholas Kirkwood, Paul Mulvaney, Asaph Widmer-

Cooper, and Tobias Kraus. Colloidal Stability of Apolar Nanoparticles: Role of Ligand Length. *Langmuir*, 34(43):12982–12989, 2018. ISSN 0743-7463. doi: 10.1021/acs.langmuir.8b02883.

28. Debora Monego, Thomas Kister, Nicholas Kirkwood, David Doblas, Paul Mulvaney, Tobias Kraus, and Asaph Widmer-Cooper. When Like Destabilizes Like: Inverted Solvent Effects in Apolar Nanoparticle Dispersions. *ACS Nano*, 14(5):5278–5287, May 2020. ISSN 1936-0851. doi: 10.1021/acsnano.9b03552. Publisher: American Chemical Society.
29. Thomas Kister, Debora Monego, Paul Mulvaney, Asaph Widmer-Cooper, and Tobias Kraus. Colloidal stability of apolar nanoparticles: the role of particle size and ligand shell structure. *ACS nano*, 12(6):5969–5977, 2018.
30. James R. Heath, Charles M. Knobler, and Daniel V. Leff. Pressure/Temperature Phase Diagrams and Superlattices of Organically Functionalized Metal Nanocrystal Monolayers: The Influence of Particle Size, Size Distribution, and Surface Passivant. *The Journal of Physical Chemistry B*, 101(2):189–197, January 1997. ISSN 1520-6106, 1520-5207. doi: 10.1021/jp9611582.
31. Uzi Landman and W. D. Luedtke. Small is different: energetic, structural, thermal, and mechanical properties of passivated nanocluster assemblies. *Faraday Discussions*, 125(0): 1–22, November 2004. ISSN 1364-5498. doi: 10.1039/B312640B.
32. W. D. Luedtke and Uzi Landman. Structure and Thermodynamics of Self-Assembled Monolayers on Gold Nanocrystallites. *The Journal of Physical Chemistry B*, 102(34):6566–6572, August 1998. ISSN 1520-6106. doi: 10.1021/jp981745i.
33. Philipp Schapotschnikow and Thijs J. H. Vlugt. Understanding interactions between capped nanocrystals: Three-body and chain packing effects. *The Journal of Chemical Physics*, 131 (12):124705, September 2009. ISSN 0021-9606. doi: 10.1063/1.3227043.
34. Claire Goldmann, Chiara Moretti, Benoit Mahler, Benjamin Abécassis, Marianne Impéror-Clerc, and Brigitte Pansu. Precise size control of hydrophobic gold nanoparticles in the 2–5 nm range. *Chemical Communications*, 57(93):12512–12515, 2021.
35. Mathias Brust, Merryl Walker, Donald Bethell, David J Schiffrin, and Robin Whyman. Synthesis of thiol-derivatised gold nanoparticles in a two-phase liquid–liquid system. *Journal of the Chemical Society, Chemical Communications*, (7):801–802, 1994.
36. Nanfeng Zheng, Jie Fan, and Galen D Stucky. One-step one-phase synthesis of monodisperse noble-metallic nanoparticles and their colloidal crystals. *Journal of the American Chemical Society*, 128(20):6550–6551, 2006.
37. Sheng Peng, Youngmin Lee, Chao Wang, Hongfeng Yin, Sheng Dai, and Shouheng Sun. A facile synthesis of monodisperse au nanoparticles and their catalysis of co oxidation. *Nano research*, 1(3):229–234, 2008.
38. Yiqun Zheng, Xiaolan Zhong, Zhiyuan Li, and Younan Xia. Successive, seed-mediated growth for the synthesis of single-crystal gold nanospheres with uniform diameters controlled in the range of 5–150 nm. *Particle & Particle Systems Characterization*, 31(2):266–273, 2014.
39. Florian Schulz, Ondřej Pavelka, Felix Lehmkühler, Fabian Westermeier, Yu Okamura, Niclas S Mueller, Stephanie Reich, and Holger Lange. Structural order in plasmonic superlattices. *Nature communications*, 11(1):1–9, 2020.
40. Florian Schulz, Torge Homolka, Neus G Bastus, Victor Puntes, Horst Weller, and Tobias Vossmeyer. Little adjustments significantly improve the turkevich synthesis of gold nanoparticles. *Langmuir*, 30(35):10779–10784, 2014.
41. Bing-Hui Wu, Hua-Yan Yang, Hua-Qi Huang, Guang-Xu Chen, and Nan-Feng Zheng. Solvent effect on the synthesis of monodisperse amine-capped au nanoparticles. *Chinese Chemical Letters*, 24(6):457–462, 2013.
42. Samuel W. Winslow, James W. Swan, and William A. Tisdale. The Importance of Unbound Ligand in Nanocrystal Superlattice Formation. *Journal of the American Chemical Society*, 142(21):9675–9685, May 2020. ISSN 0002-7863. doi: 10.1021/jacs.0c01809.
43. Wojciech Kwieciński, Tim Segers, Sjoerd van der Werf, Arie van Houselt, Detlef Lohse, Harold J. W. Zandvliet, and Stefan Kooij. Evaporation of Dilute Sodium Dodecyl Sulfate Droplets on a Hydrophobic Substrate. *Langmuir*, 35(32):10453–10460, August 2019. ISSN 0743-7463, 1520-5827. doi: 10.1021/acs.langmuir.9b00824.
44. Michael A Boles and Dmitri V Talapin. Many-body effects in nanocrystal superlattices: departure from sphere packing explains stability of binary phases. *Journal of the American Chemical Society*, 137(13):4494–4502, 2015.
45. Curt Waltmann, Nathan Horst, and Alex Travesset. Potential of mean force for two nanocrystals: Core geometry and size, hydrocarbon unsaturation, and universality with respect to the force field. *The Journal of Chemical Physics*, 149(3):034109, July 2018. ISSN 0021-9606. doi: 10.1063/1.5039495.
46. Johann Lacava, Anika Weber, and Tobias Kraus. Ageing of alkylthiol-stabilized gold nanoparticles. *Particle & Particle Systems Characterization*, 32(4):458–466, 2015.
47. CJ Kiely, J Fink, M Brust, D Bethell, and DJ Schiffrin. Spontaneous ordering of bimodal ensembles of nanoscopic gold clusters. *Nature*, 396(6710):444–446, 1998.
48. Yuan Cao, Valla Fatemi, Shiang Fang, Kenji Watanabe, Takashi Taniguchi, Efthimios Kaxiras, and Pablo Jarillo-Herrero. Unconventional superconductivity in magic-angle graphene superlattices. *Nature*, 556(7699):43–50, April 2018. ISSN 1476-4687. doi: 10.1038/nature26160.
49. Rafi Bistritzer and Allan H. MacDonald. Moiré bands in twisted double-layer graphene. *Proceedings of the National Academy of Sciences*, 108(30):12233–12237, July 2011. doi: 10.1073/pnas.1108174108.
50. Elizabeth Gibney. How 'magic angle' graphene is stirring up physics. *Nature*, 565(7737): 15–18, January 2019. doi: 10.1038/d41586-018-07848-2.
51. G Viau, R Brayner, L Poul, N Chakroune, Emmanuelle Lacaze, F Fievet-Vincent, and F Fievet. Ruthenium nanoparticles: size, shape, and self-assemblies. *Chemistry of Materials*, 15(2):486–494, 2003.
52. Rashmeet Kaur Khurana. Moiré patterns in nanomaterials. *Materials Science in Semiconductor Processing*, 140:106406, March 2022. ISSN 1369-8001. doi: 10.1016/j.mssp.2021.106406.
53. Ajay Singh, Calum Dickinson, and Kevin M. Ryan. Insight into the 3D Architecture and Quasicrystal Symmetry of Multilayer Nanorod Assemblies from Moiré Interference Patterns. *ACS Nano*, 6(4):3339–3345, April 2012. ISSN 1936-0851. doi: 10.1021/nn300331x.
54. Cyrille Hamon, Sergey M. Novikov, Leonardo Scarabelli, Diego M. Solís, Thomas Altantzis, Sara Bals, José M. Taboada, Fernando Obelleiro, and Luis M. Liz-Marzán. Collective Plasmonic Properties in Few-Layer Gold Nanorod Supercrystals. *ACS Photonics*, 2(10):1482–1488, October 2015. doi: 10.1021/acsphotonics.5b00369.
55. Brian A Korgel, Stephen Fullam, Stephen Connolly, and Donald Fitzmaurice. Assembly and self-organization of silver nanocrystal superlattices: Ordered "soft spheres". *The Journal of Physical Chemistry B*, 102(43):8379–8388, 1998.
56. Kai Chen, Bharath Bangalore Rajeeva, Zilong Wu, Michael Rukavina, Thang Duy Dao, Satoshi Ishii, Masakazu Aono, Tadaaki Nagao, and Yuebing Zheng. Moiré Nanosphere Lithography. *ACS Nano*, 9(6):6031–6040, June 2015. ISSN 1936-0851. doi: 10.1021/acsnano.5b00978.
57. Wolfgang Haiss, Nguyen TK Thanh, Jenny Aveyard, and David G Fernig. Determination of size and concentration of gold nanoparticles from uv- vis spectra. *Analytical chemistry*, 79 (11):4215–4221, 2007.
58. Jan Ilavsky. Nika: software for two-dimensional data reduction. *Journal of Applied Crystallography*, 45(2):324–328, 2012.